Validation of the Similar Particle Assembly (SPA) Model for the Fluidization of Geldart's Group A and D Particles

M. A. Mokhtar, K. Kuwagi, and T. Takami
Dept. of Mechanical Systems Engineering, Faculty of Engineering, Okayama University of Science, Ridai-Cho 1-1, Okayama 700-0005, Japan

H. Hirano
Dept. of Biotechnology and Applied Chemistry, Faculty of Science, Okayama University of Science, Ridai-Cho 1-1, Okayama 700-0005, Japan

M. Horio
Research Institute of Science and Technology for Society (RISTEX), Japan Science and Technology Agency (JST), Ohte-machi 1-1-2, Chiyoda-ku, Tokyo 100-0004, Japan

DOI 10.1002/aic.12568
Published online April 18, 2011 in Wiley Online Library (wileyonlinelibrary.com).

The similar particle assembly (SPA) model proposed for large-scale discrete element method simulation was validated. The SPA model describes the scaling law for the motion of particles in an assembly, which is derived from the equation of motion of a particle. In the SPA model, particles with similar physical or chemical properties are represented by a single particle, which is called the representative particle. The local assembly of particles in the original bed is supposed to be maintained in the bed with the representative particles. The SPA model was validated by numerical simulations of a 2D fluidized bed of noncohesive and cohesive particles. Using the SPA model, the flow behavior of the representative particles of a certain magnification can be made similar to that of the original particles with significantly less computational load. A good approximation of bubble size distribution between the SPA bed and the original bed was obtained. © 2011 American Institute of Chemical Engineers *AIChE J,* 58: 87–98, 2012

Keywords: discrete element method, fluidized bed, bubbling fluidization, homogeneous fluidization, bubble analysis

Introduction

Although industrial processes that deal with particles and powders are often beset by the innate problems caused by the undesired behavior of particulate matters, significant progress in the numerical description of particulate systems has continued as a result of the development of the discrete element method (DEM). The original DEM concept based on the soft sphere contacts was derived by Cundall and Strack[1] in the field of geomechanics. The DEM simulation technique has gained serious attention from academia and has spread through multiscale industries in which powder technology is applied. The key feature of the DEM is the ability to account for several realistic behaviors of particulate systems in numerical analyses, for example, in agglomeration[2] and dust removal.[3] Following the work of Tsuji et al.,[4] several

Correspondence concerning this article should be addressed to K. Kuwagi at kuwagi@mech.ous.ac.jp.

researchers have attempted to incorporate real-world problems that occur in industrial fluidization processes into DEM simulations. These include cohesive forces, which mainly cause agglomeration and/or clinker formation. Mikami et al.[5] developed a numerical simulation code called simulation of agglomerating fluidization for industrial reaction engineering (SAFIRE) whick took into account the liquid bridging force. For metallic surface diffusion sintering, i.e., solid bridging force, Kuwagi et al.[6] simulated the process of sintering agglomerates and defluidization using the relationship between the neck growth time and the neck radius derived by Kuczynski.[7]

Cohesive forces are not the only cause of problems in industrial processes that deal with particles and powders. Rong and Horio[8] developed the SAFIRE Ver. 6 simulation code for particle collision heat transfer and solid combustion. They successfully analyzed the thermodynamic characteristics and NO_x emission of burning chars in a fluidized bed. These studies and others,[9–11] have demonstrated the capability of the DEM as a powerful tool for investigating practical problems that occur in industrial particulate processes. However, a major hurdle exists for the large-scale application of the DEM because a very limited number of particles are considered in typical single-CPU simulation. A particulate system usually contains a large number of ''elements'' or simply particles. In fact, for practical-scale reactors, a number of elements on the order of one billion is often required to treat such systems in DEM simulations. If the detailed behavior of the particles on such a scale is to be simulated, then the complexity and volume of DEM analysis will create bottlenecks in computer performance. Since the DEM is a Lagrangian method that uses intensive procedures to track every particle in the system based on Newton's second law of motion, the simulation of a large number of particles would require an unacceptable computational time, which is the most significant drawback of existing DEM methods.

With the exponential growth in computing performance,[12,13] supercomputers with parallel computing technology can be used in the analysis of discrete particulate systems, in which a huge number of elements, i.e., particles, can be treated. For example, Tsuji et al.[14] simulated more than 4.5 million particles by parallel computing using 16 processors and reported the spontaneous structures in 3D bubbling fluidization. Despite the remarkable capability of the supercomputers, parallel computing may sometimes not be adequate for handling the modeling of certain complex configurations in fluid flow, which cannot be easily decomposed and executed efficiently by parallel computing.[15] As computer performance advances, a soft approach to large-scale simulation problems should also be considered. However, what type of numerical algorithm should be developed? For instance, if the particle phase is treated with the Eulerian method, as in the case of a two-fluid model (TFM),[16] the computational load is not as high as that associated with the DEM because the particle phase is independent of the number of particles. The direct simulation Monte Carlo (DSMC) method is also a well-known approach for reducing the number of particles. However, due to inter-particle cohesion forces, it is difficult to treat the primary problems, such as the agglomeration, using the TFM or by the DSMC method.

A number of models for the DEM have been derived for the simulation of a large number of particles. Kazari et al.[17] proposed similarity conditions for particle motion and carried out simulations using particles of different diameter to investigate their validity. However, good agreement was not obtained for the pressure drop or the bubble behavior. Sakano et al.[18] derived a model called the imaginary sphere model, in which an imaginary sphere with a greater diameter and a lower density was compared with actual particles, assuming a face centered cubic structure of particles. However, the bubble diameter obtained from the simulation using the imaginary sphere model was smaller than the experimentally obtained diameter. Moreover, it appears to be difficult to apply the imaginary sphere model to realistic systems because the meaning and validation of the assumed particle structure in an imaginary sphere have not been clearly described. Takeda and Horio[19] proposed a hybrid model of the DEM and the TFM. In the hybrid model, sample grids as large as the grid of the TFM are introduced for DEM analysis in computational cells to solve the average cell physical quantities. Here, DEM simulation is performed using a sample grid with periodic boundary conditions to provide the average cell physical quantities and stress tensors due to contact forces between particles. The most difficult problems associated with the hybrid model are the treatment of cell size in accordance with the bed expansion and the particle acceleration in the periodic boundary conditions. Since the hybrid model is currently still under development, its practical usefulness cannot be determined yet. Snider[20] presented a multiphase particle-in-cell (MP-PIC) method for dense particle flows in which solids pressure gradient is considered in the particle equation of motion, instead of the collision forces (soft-sphere and/or hard-sphere models). Particles were implicitly coupled to the fluid phase where fluid momentum and pressure equations are implicitly solved. By avoiding the implicit calculation of particle normal stress on the grid using a subgrid particle, the method provides a fast solution for a large particle population. However, Benyahia and Galvin[21] showed that large numerical errors are found in the MP-PIC method and other methods that employing the concept of computational parcel (contains set of particles moving at the same velocity) while studying their time-averaged flow variables.

To obtain a rational technique for dealing with large-scale DEM simulation, a rigorously derived scaling law is proposed. The present study incorporates a particle scaling law in the governing equations of the DEM using the similar particle assembly (SPA) model developed by Kuwagi et al.[22] Sakai et al.[23,24] used coarse grain model for a large DEM simulation in which particle–particle and particle-fluid interaction forces are based on the SPA approach. Moreover, they described the modeling approach in rotational direction. However, the deviations of coarse grain model on different flow regimes are not reported.

Accordingly, the present paper describes a series of DEM simulation results used to validate the applicability and limits of the SPA model for the fluidization simulation of Geldart's Group A and Group D particles. The investigation of fluidization behaviors for both the original system (without the SPA model) and the system represented by the SPA model are first described, followed by the bubble analyses, which consider the variation of voidages around bubbles.

Numerical Technique

Governing equations for DEM simulation

The most attractive feature of the DEM is the capability to investigate phenomena that occur on the scale of single particle, where the number of particles N_p is the key factor influencing the calculation speed. For large-scale simulation, this will require DEM simulation to consume an enormous amount of time due to the execution of numerous calculation steps. To overcome this disadvantage, we attempt to use a model that can reduce the number of particles without severely altering the actual behavior, as if the simulation were conducted using a large number of particles. The following discussion outlines the important equations required for DEM simulation, followed by the derivation of the SPA model.

General DEM simulation requires the motion of the fluid (gas) phase to be solved using the locally averaged Navier-Stokes equations.[25] These equations describe the conservative form for the mass and the momentum of the fluid. To express the continuity equation for mass conservation, we write

$$\frac{\partial(\varepsilon\rho_f)}{\partial t}+\nabla(\varepsilon\rho_f \boldsymbol{u})=0, \tag{1}$$

where ε is the fluid voidage and $\boldsymbol{u}$ is the upward superficial fluid velocity. The following equation denotes the momentum conservation of fluid:

$$\frac{\partial(\varepsilon\rho_f \boldsymbol{u})}{\partial t}+\nabla(\varepsilon\rho_f \boldsymbol{u}\boldsymbol{u})=-\varepsilon\nabla p+\boldsymbol{F}_f+\varepsilon\rho_f \boldsymbol{g} \tag{2}$$

In the right-hand side of the above equation, $\boldsymbol{F}_f$ represents the force acting on the fluid cell from the particles. On the other hand, the particle motion is based on Newton's equation of motion and is described using the Lagrangian approach with two-way coupling between the fluid phase and the particle phase. This equation takes the following form:

$$\rho_{p(i)}\left(\frac{\pi}{6}d_{p(i)}^3\right)\frac{d\boldsymbol{v}_{(i)}}{dt}=\sum_{i\neq j}\boldsymbol{F}_{p(ij)}+\boldsymbol{F}_{fp(i)}+\rho_{p(i)}\left(\frac{\pi}{6}d_{p(i)}^3\right)\boldsymbol{g}+\boldsymbol{F}_{coh} \tag{3}$$

where $\rho_{p(i)}$ is the particle density, d_p is the particle diameter, and i,j denotes the particle indices. For non-cohesive bed operation, the equation of motion for each particle is balanced by the contact force between two particles $\boldsymbol{F}_{p(ij)}$, the fluid-particle interaction force $\boldsymbol{F}_{fp(i)}$, and the gravitational force. The contact force $\boldsymbol{F}_{p(ij)}$ between two contacting particles is defined by the soft sphere model.[1] The contact force can be decomposed into the normal force $\boldsymbol{F}_n$ and the tangential force $\boldsymbol{F}_t$, as shown in the following equations:

$$\boldsymbol{F}_n=-k_n\boldsymbol{x}_n-\eta\frac{d\boldsymbol{x}_n}{dt} \tag{4}$$

$$\boldsymbol{F}_t=-k_t\boldsymbol{x}_t-\eta\frac{d\boldsymbol{x}_t}{dt}\quad |\boldsymbol{F}_t|<\mu|\boldsymbol{F}_n| \tag{5}$$

where $\boldsymbol{x}_n$ and $\boldsymbol{x}_t$ are the overlap distance between the interacting particles, and k_n and k_t are the spring stiffness coefficients in the normal and tangential directions, respectively. In addition, the viscous damping coefficient and the friction coefficient are indicated by η and μ, respectively. If friction due to sliding occurs, the following equation should be applied:

$$\boldsymbol{F}_t=-\mu|\boldsymbol{F}_n|\frac{\boldsymbol{x}_t}{|\boldsymbol{x}_t|}\quad |\boldsymbol{F}_t|>\mu|\boldsymbol{F}_n| \tag{6}$$

The force caused by the tangential contact gives the particle a rotational motion. Thus, the torque balance equation for the rotational motion of the particle can be given by

$$I\frac{d\boldsymbol{\omega}}{dt}=\boldsymbol{F}_t\cdot r_p \tag{7}$$

where I is the moment of inertia and $\boldsymbol{\omega}$ is the angular velocity of the particle. For cohesive bed operation, the equation for the liquid bridge force[5] $\boldsymbol{F}_{coh}$ was added to the equation of motion for particles in the following form:

$$\widehat{\boldsymbol{F}}_{coh}=\frac{\boldsymbol{F}_{coh}}{\pi r_p\gamma_c} \tag{8}$$

$\widehat{\boldsymbol{F}}_{coh}$ is the dimensionless liquid bridge force and can be defined as

$$\widehat{\boldsymbol{F}}_{coh}=\exp(A\hat{h}_c+B)+C \tag{9}$$

where A, B, C, and $\hat{h}_c$ are dimensionless parameters in the function of dimensionless liquid volume, $\hat{V}$. Simulation of the liquid bridge force is based on the assumption that when a particle contacts another particle, a thin bridge of liquid (water in this case) with a given volume, $V(=\hat{V}r_p^3)$ is immediately formed at the contact point. Comprehensive details on the liquid bridge force can be found in a study by Mikami et al.[26] and others.[27–30]

Derivation of the SPA model

First, let us consider a bed of particles and name this bed the original system, which contains original particles i of diameter d_p, as shown in Figures 1a,c. These particles are grouped together in which their size, density, and chemical composition are similar. Their velocity and the direction of motion are also similar. A representative system is a system of particles, which contains a set of representative particles i' that are assumed to occupy an equal space (bed) size. However, the representative system represents the performance or behavior of the original system but with fewer particles, as shown in Figure 1b,d. Here, it is assumed that particle i', which corresponds to particle i, exists in the m times larger system. If the voidage and the existence fraction of the particle group are the same around particle i, the space arrangement of the original system and that of the representative system become analogous, i.e., a similar particle assembly model can be established.

Specifically, the behavior of the representative system is similar to that of the original system in that the local assembly of particles including local voidage and the coordination of different particle species and velocity are similar between the original and represented systems. Since the space

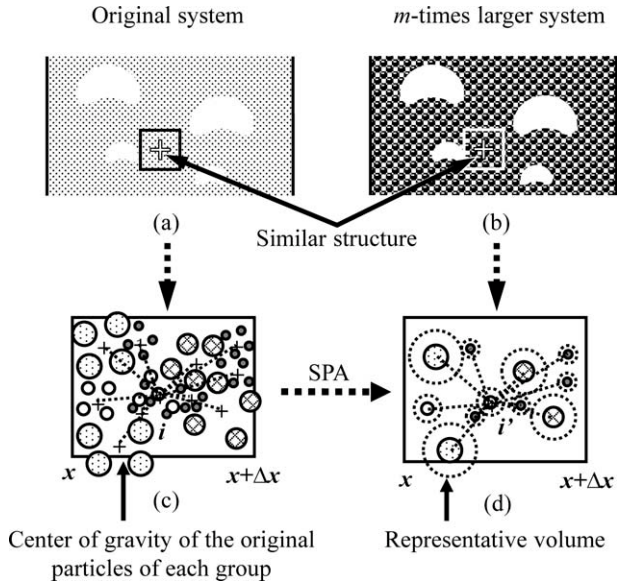

Figure 1. Diagram of the scaling law for the similar particle assembly (SPA) model.

occupied by n particles is represented by a representative particle of group k, which moves together with the representative particle at the center of the represented volume, the diameter of the space represented by particle i in group k can be written as follows:

$$md_{\mathrm{pk}} = \sqrt[3]{n}(d_{\mathrm{pk}}) \tag{10}$$

Next, by considering that representative particle i' has a volume that is m times larger than the original particle i, the following scaling equation can be obtained:

$$d_{\mathrm{p}(i')} = md_{\mathrm{p}(i)} \tag{11}$$

Here, the representative particle number is calculated to be $N_{\mathrm{p}}^{1/3}$ times smaller the than original particle number. The equation corresponding to Eq. 3 in the m times larger system becomes as follows:

$$m^3\rho_{\mathrm{p}(i')}\left(\frac{\pi}{6}d_{\mathrm{p}(i)}^3\right)\frac{d\boldsymbol{v}_{(i')}}{dt} = \sum_{i'\neq j'}\boldsymbol{F}^*_{\mathrm{p}(i'j')} + \boldsymbol{F}^*_{\mathrm{fp}(i')} + m^3\rho_{\mathrm{p}(i')}\left(\frac{\pi}{6}d_{\mathrm{p}(i)}^3\right)\boldsymbol{g} \tag{12}$$

Here, since the particle diameter has a major impact on the hydrodynamic behavior of the particle, the scaling law can be applied directly to particle–particle and particle-fluid interaction forces, as shown below:

$$\sum_{i'\neq j'}\boldsymbol{F}^*_{\mathrm{p}(i'j')} + \boldsymbol{F}^*_{\mathrm{fp}(i')} = m^3\left(\sum_{i\neq j}\boldsymbol{F}_{\mathrm{p}(ij)} + \boldsymbol{F}_{\mathrm{fp}}\right) \tag{13}$$

If $d_{\mathrm{p}(i')}$ is used to calculate $\boldsymbol{F}^*_{\mathrm{p}(i'j')}$ and $\boldsymbol{F}^*_{\mathrm{fp}(i')}$ in Eq. 12, it is difficult to obtain the equation for $\boldsymbol{F}^*_{\mathrm{p}(i'j')}$ and $\boldsymbol{F}^*_{\mathrm{fp}(i')}$ that satisfies Eq. 13. However, if $d_{\mathrm{p}(i)}$ is used, Eq. 13 is easily satisfied. Then, if Eq. 13 is satisfied and the density of the space represented by a representative particle is the same as the original particle, i.e., $\rho_{\mathrm{p}(i')} = \rho_{\mathrm{p}(i)}$, then the velocity congruity can be established by further comparing Eqs. 3 and 12 to obtain

$$\boldsymbol{v}_{(i')} = \boldsymbol{v}_{(i)}. \tag{14}$$

Equation 14 indicates that the particle in the m times larger system has a movement that is similar to the movement of the corresponding original particles. Hence, the SPA model assumptions between the original system and the system represented by m times larger particles hold. Note that the macroscopic fluidization behaviors of both the original and representative particles systems are not analogous but are congruent to one another with some difference in resolutions, as shown previously in Figures 1a,b. Moreover, the detection of contacts or collisions between particles is performed using the diameter of the representative volume $d_{\mathrm{p}'}$ to maintain realistic interactions between particles in the SPA model. However, when we calculate particle-particle $\boldsymbol{F}^*_{\mathrm{p}(i'j')}$ and fluid-particle $\boldsymbol{F}^*_{\mathrm{fp}(i')}$ interaction forces, the physical properties of the original particles must be used. This is the most important feature of the present model. Furthermore, the force acting on fluid $\boldsymbol{F}_{\mathrm{f}}$ becomes the same if the voidage ε is the same as that of the original system. As the SPA model can be applied directly to every term in the equation of motion for particle phase, many other models describing the interactions between particle–particle and particle-fluid in the DEM simulation can take this advantage. This includes the cohesion (liquid bridge, van der Waals) force model, the lubrication force model and heat transfer model. For 3D SPA model, Kuwagi et al.[31] conducted a DEM simulation for a gas-particle dispersion system at high temperature and successfully quantized the cohesive force between thermoset particles.

Numerical Simulation Procedures

Analysis parameters

Validation of the SPA model is carried out in a series of numerical simulations for 2D rectangle fluidized bed operation with both noncohesive and cohesive particles. For a side-by-side comparison, the general formulation of the DEM was used in the original particle system, whereas the SPA model formulation was used in the representative system with three and six times magnification. Particles belonging to Geldart's[32] Group A (fine particles of 0.1 mm in diameter) and Group D (coarse particles of 1.0 mm in diameter) are chosen. First, the code for the SPA model was obtained through the modification of the SAFIRE code.[26] Accordingly, the elastic repulsion force is expressed as $\boldsymbol{F}_{\mathrm{p}(ij)}$ using Hooke's law, and the particle-fluid interaction force is calculated using the Wen and Yu correlation[33] for a dilute suspension and the Ergun[34] equation for a dense bed ($\varepsilon < 0.8$). For the fluidization of cohesive particles, the dimensionless constant parameter $\hat{V}$ was set to 1.0×10^{-2} to represent the volume of the liquid bridge, providing the equivalent of 0.27 wt % water for the wet bed condition. In

Table 1. Simulation Parameters

Parameter	Group A	Group D
Bed dimensions, $W \times H$ (m)	0.05×0.15	0.5×1.5
Particle diameter, d_p (mm)	0.1*, 0.3†, 0.6‡	0.1*, 3.0†, 6.0‡
Particle density, ρ_p (kg/m^3)	800	2650
Fluid superficial velocities, u_0 (m/s)	0.008(homogenous), 0.03(bubbling).	1.2
Particle number, N_b(-)	270,000*; 30,000†; 7,500‡	
Particle restitution coefficient, e (-)	0.9	
Particle friction coefficient, μ (-)	0.3	
Spring constant, K (N/m)	800	
Fluid density, ρ_f (kg/m^3)	1.15	
Fluid viscosity, μ_f (Pa s)	1.75×10^{-5}	
Dimensionless liquid volume, $\hat{V}$(-)		1.0×10^{-2}
Surface tension, γ_c (N/m)		0.073
Contact angle, θ_c (rad)		0

*Original.
†SPA - three times magnification.
‡SPA - six times magnification.

addition, a dimensionless parameter called the critical rupture distance $\hat{h}_c$ controls whether the liquid bridge ruptures or remains intact. If the liquid bridge remains intact, then the liquid bridge force, as well as other cohesive forces (if considered), contribute to the agglomerate build-up.

The total number of particles N_p used to represent the original systems of Geldart's Group D and Group A is 270,000 particles. The corresponding representative systems were constructed using three and six times magnification based on the SPA model descriptions. This leads to a magnification of the original d_p from 1.0 mm to 3.0 and 6.0 mm for Group D and from 0.1 mm to 0.3 and 0.6 mm for Group A. The total particle number N_p of the original system is then reduced to 30,000 and 7500 particles with three- and six-times magnification, respectively. For simplified notation, the original system and the representative systems are hereinafter referred to as the original bed and the SPA bed(s), respectively. Further details regarding the numerical simulation parameters are listed in Table 1. The parameters associated with the particles in the original bed are mostly from Mikami.[26]

All of the governing equations are solved in a pseudo-2D Cartesian coordinate system, in which the depth of the bed is equal to the diameter of a single particle. In the simulation, the finite difference method (FDM) is adopted in the spatial discretization procedure, whereas the SIMPLE[35] scheme is used to solve the pressure field. For numerical convenience in the DEM calculation, the spring stiffness is set to be 800 N/m. Since the contact force in the DEM is modeled by the spring-damper system, the problem of the spring constant value arises in the present model. In the general DEM simulations, the spring constant has little effect on the flow behavior.[26] Thus, the value of the spring constant can be set arbitrarily. However, in the SPA model, the spring constant should be set carefully, so that the displacement of particles, as well as the calculation of the time step, becomes similar to the original system.

Influence of voidage variations on the bubble size distribution

It is important to determine the voidage at the contour line around a bubble ε_{bcl} to define the bounded area of the bubble when the numerical results are compared in terms of bubble size distribution. ε_{bcl} varies during the transition from the bubbling phase (gas bubbles) to the particulate phase (fluidized particles around the bubbles). Figure 2 shows how the variation of ε_{bcl} influences the size of the bubbles. The variation of ε_{bcl}, which is calculated for each fluid cell, shows that the size of the bubbles increases as ε_{bcl} decreases. For example, a large bubble is observed when the contour line at $\varepsilon_{bcl} = 0.6$ expanded and wrapped around the adjacent bubble. This behavior is generally interpreted as the result of bubble coalescence. Bubble analyses based on the variation of ε_{bcl} could provide a feasible method for the comparison of bubbling behaviors between the original bed and the SPA bed. This approach also addresses the inaccuracies in defining bubble size due to the coarse resolution resulting from the magnifications required by the SPA model. However, care must be taken because an inappropriate choice of the value of ε_{bcl} could bring about difficulties in determining the bubble size distribution. For example, for the case of Geldart's Group A particles, the contour line chosen at $\varepsilon_{bcl} < 0.7$ will cause greatly oversized bubbles due to contour line overlapping, as well as failure to detect small bubbles. For bubble size calculation, a snapshot of bubble visualization

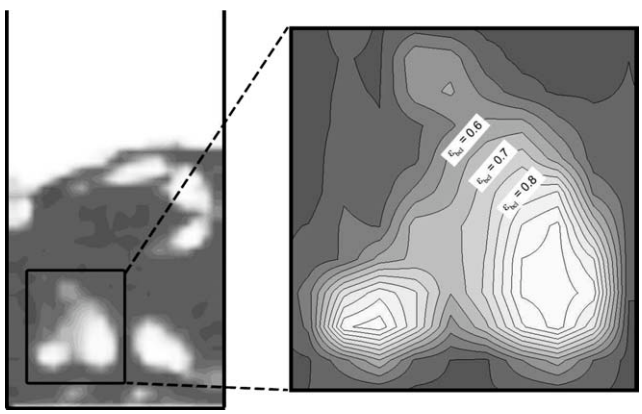

Figure 2. Variation of voidages at the contour line around bubbles, ε_{bcl}. Each ε_{bcl} significantly affects the bubble size distribution.

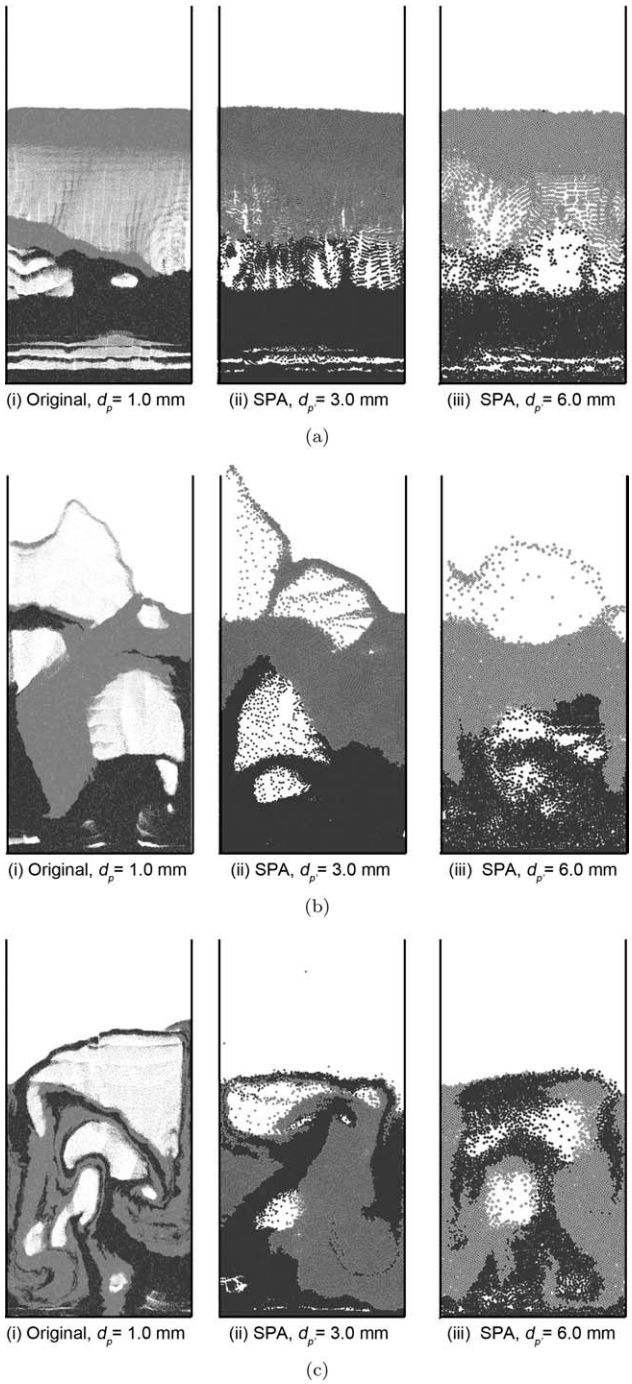

Figure 3. Comparison of fluidization behavior for Group D particles during (a) slug flow, (b) bubbling flow, and (c) particle mixing between the original bed (d_p = 1.0 mm) and the SPA beds, ($d_{p'}$ = 3.0, 6.0 mm).

was postprocessed into a gray-scale image using the thresholding method[36] to determine the variance between the gas phase and the particle phase. For geometry simplicity, the shape of a bubble was simplified to a less complex 2D circular-equivalent shape. The bubble diameter D_b was then calculated from $\sqrt{4(A_b)/\pi}$, where A_b is the area bounded by the contour line taken at ε_{bcl}.

Results and Discussions

Comparison of fluidization behavior

In the dry (noncohesive) fluidized bed, the fluid force is the only force that significantly affects the particle hydrodynamics after the gravitational force is overcome. Here, the particles fluidize and achieve different flow structures when subjected to changes in gas inlet velocity u_0. The variety of the flow structures are induced by the competition between the particle-particle and particle-gas interaction forces.[37] From the initial static bed condition, u_0 is gradually increased to 1.20 m/s for bubbling fluidization. Snapshots of the fluidization of noncohesive particles for Group D particles with the original bed (d_p = 1.0 mm) and the SPA beds ($d_{p'}$ = 3.0, 6.0 mm) are shown in Figure 3. Particles are divided into upper-half and lower-half sets and are differentiable by two color indicators. From visual inspection of Figure 3, SPA beds show macroscopically similar fluidization regimes to that of original bed. Figure 3a indicates a similar slugging phenomena at t = 0.79 sec, in which gas slugs approximately the size of the bed width can be observed at the lower-half regime of both the original and the SPA beds. Despite the difficulty in obtaining identical motions with respect to instantaneous time due to random particle motions, both the 3.0 mm and 6.0 mm SPA beds exhibit remarkably similar splashes (burst of particles) caused by bubble eruptions near the bed surface at t = 1.31 sec (Figure 3b). Furthermore, SPA bed ($d_{p'}$ = 3.0 mm) display a well defined particulate-bubble flow structure similar to original particles in which particle–particle interaction forces dominate particle-gas interaction forces. However, the poor approximation of bubbly flow structure by the SPA bed ($d_{p'}$ = 6.0 mm) indicate that there is relatively weaker particle–particle interaction forces in the SPA model with six times magnification. As magnification times increases, the number of particles decreases of which causing less particle-particle interaction forces.

The minimum fluidization velocity u_{mf} can be influenced by the compact construction of particles under the static bed condition, in which there is the possibility of overshoot in ΔP. To ensure that the value of u_{mf} is accurate, defluidization is carried out by gradually decreasing the gas velocity u_0 from a fully-developed bubbling fluidized bed. The minimum fluidization velocity, u_{mf} is listed in Table 2. For Geldart's Group D particles, u_{mf} for the SPA beds closely matches that of the original bed, which is taken to be 0.65 m/s. On the other hand, for Geldart's Group A particles, u_{mf} for the SPA beds is ~0.003 m/s. The u_{mf} values are ~16% (for Group D) and 11% (for Group A) larger than those predicted by the Wen and Yu correlation. This would be caused by particle arrangement in pseudo 2D bed columns.

Due to the magnification of particle diameter required by the SPA scaling law, it was expected that deterioration in particle mixing behavior would occur (Figure 3c). The

Table 2. Minimum Fluidization Velocity

Geldart's Classification	u_{mf} (m/s) by Wen and Yu[33]	u_{mf} (m/s) by Original/SPA
Group D particles (d_p = 1.0 mm)	0.57	0.65 0.70 (wet)
Group A particles (d_p = 0.1 mm)	0.0027	0.003

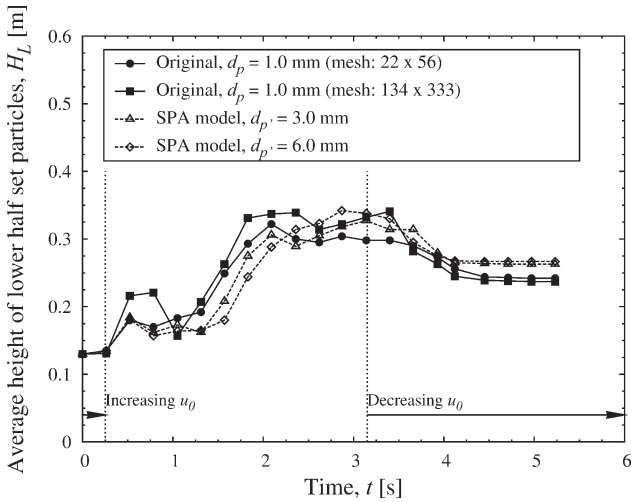

Figure 4. Average height of lower-half set particles obtained during noncohesive fluidization of Geldart's Group D particles.

results was taken at $t = 2.36$ sec for the SPA beds (Geldart's Group D) reveal that the particles in the lower-half region fluidize in less chaotic motion with the presence of bulky circulation flow patterns. In addition, the SPA beds appear to require a longer time to reach a high degree of particle mixing, as compared to the original bed. For Group D particles, this is identical to the case in which particles larger than 1 mm in diameter tend to fluidize unevenly. However, since all of the particles in the SPA models are tagged with their original particle indexes, as described in "Numerical Technique" section, these particles should able to retain their macroscopic local assembly and local voidage with respect to the original particle system. Figure 4 verifies the degree to which SPA models for Group D particles fluidize differently from the original particles by calculating the average height of lower-half set particles throughout the fluidization process. The results indicate fair qualitative agreement for SPA beds, in which particles initially located in the lower-half bed regime yield a prediction close to the average height history of the original bed. The calculated error falls between 5 and 9%, which is acceptable, although the mixing breakthrough occurs slightly late. This is because the bubble size in the SPA beds was small compared to the bubble size in original bed. However, this difference is approximately the same as that caused by the influence of the fluid mesh size, as indicated by the broken line in Figure 4.

Homogenous fluidization

As a result of the broad applicability of the SPA model, we extend our analysis to homogenous fluidization, which usually occurs in the fluidization of Group A particles.[32] This phenomenon normally becomes apparent in fine particles[38] and is extensively discussed in the literature.[39,40] Figure 5 compares the homogeneous fluidization of the original bed ($d_p = 0.1$ mm) and the SPA beds ($d_{p'} = 0.3$, 0.6 mm) for Group A particles simulated from the initial static bed until $u_0 = 0.008$ m/s is reached and maintained constant for a certain period, during which the bed expansion behavior can be observed. Unlike the Group D particles, the Group A particles exhibit continuous bed expansion with upward breakthroughs of the lower-layer particles at $t = 1.14$ sec (Figure 5a). When the gas velocity is gradually increased to a velocity range of $u_{mf} < u_0 < u_{mb}$, at which homogeneous expansion occurs,[41] the particles begin to move progressively, but remain close to one another, in the direction of the gas flow. As a result, the bed expands and initiates the particle mixing action without the presence of disturbances such as bubbles (Figure 5b).

Figure 6 shows the average height of the lower-half set particles calculated for the homogeneous fluidization. In the incipient fluidized state, the original bed ($d_p = 0.1$ mm) exhibits the earliest mixing breakthrough, which originates from the center of the bed at $t = 0.22$ s, but is not significant until $t = 0.68$ s for the SPA bed with $d_{p'} = 0.3$ mm and $t = 1.14$ s for the SPA bed with $d_{p'} = 0.6$ mm. Despite the difference in mixing breakthrough time, the onset of particle chaotic mixing is similar, $\sim t = 1.85$ s. However, H_L plotted from $t = 1.80$ s indicates that the average height of the three beds is comparable. As the magnification increases, the SPA beds preserve the static (no mixing) expansion for a slightly longer period. Here, the rotational motion in the

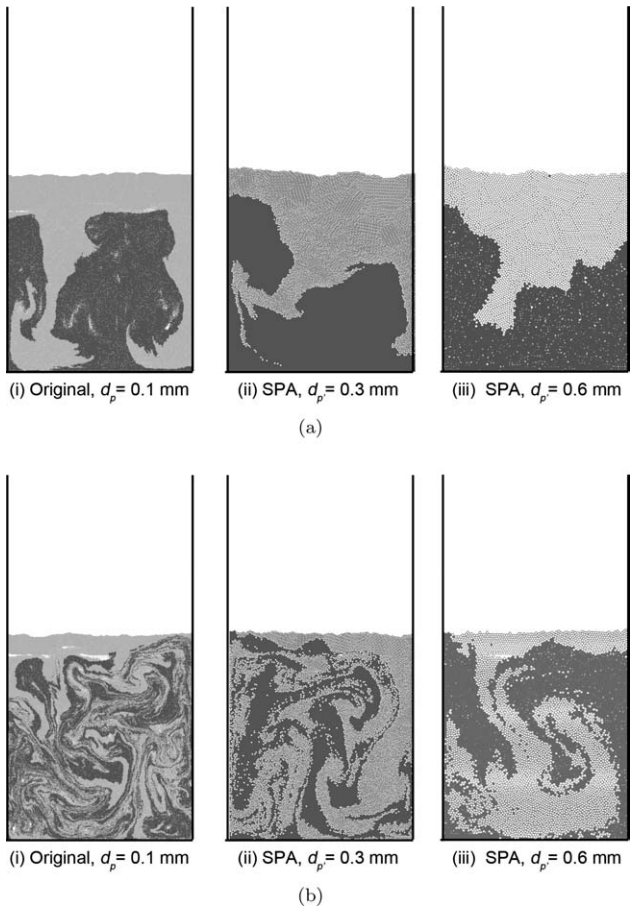

Figure 5. Comparison of homogeneous fluidization behavior for Group A particles between the original bed (d_p = 0.1 mm) and the SPA beds, ($d_{p'}$ = 0.3, 0.6 mm) during (a) upward breakthrough and (b) particle mixing.

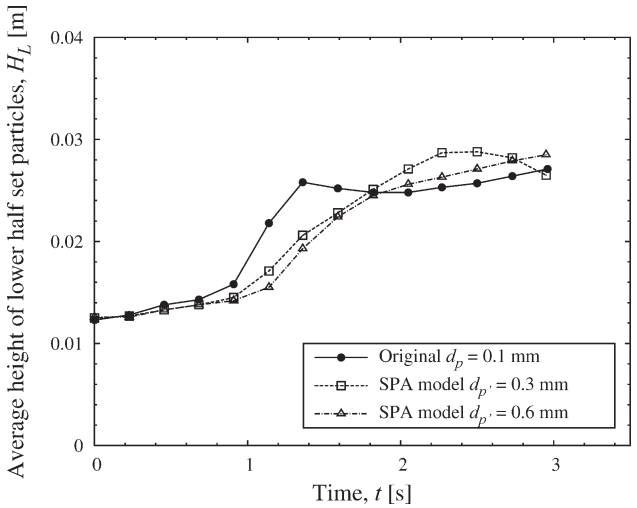

Figure 6. Average height of lower-half set particles obtained during homogeneous fluidization of Geldart's Group A particles.

SPA model must be considered because the mixing behavior during bed expansion is greatly influenced by the rotational motion of particles. As mentioned earlier, the diameter of the representative volume is used for particle contact detection in the SPA model. However, it is not practical to use the same $d_{p'}$ to define the rotational motion in the SPA model, because this will cause much smaller rotational motion, i.e., slower mixing velocity compared to the case in which d_p is used.

Bubble analyses

According to the two-phase theory of fluidization,[42] the gas required to fluidize a bed of particles can exist in excess ($u_0 - u_{mf}$) in the form of gas bubbles. Bubbles produced in a fluidized bed provide a feasible mixing action for particles due to the random unstable flow structure.[44–45] In two-dimensional bubble analyses, bubble behavior can be described in terms of the following characteristics: size (diameter) distribution, shape, wake, and rise velocity. In the present bubble analyses, priority is given to the bubble size distribution D_b and the bubble rise velocity u_b, where bubbles from the SPA beds will be compared to those from the original bed.

The change in hydrodynamic pressure allows bubbles to grow larger as they rise upward, moving further from the distributor. The rising bubbles continuously undergo coalescence and break-up, which give fluctuations to the size distributions of the bubbles. Figure 7 summarizes the bubble size distributions calculated at different values of ε_{bcl}. The data was obtained by analyzing 50 successive snapshots taken over a period of 1.28 s during bubbling. As shown in Figure 7a, a good approximation of the bubble size distribution is obtained for the original bed ($d_p = 1.0$ mm) and the SPA bed ($d_{p'} = 3.0$ mm). The wide fluctuations in the number of bubbles N_b confirm the sparse distribution of bubble sizes, which is generally associated with Geldart's Group D particles. As ε_{bcl} decreases, N_b for small bubbles also decreases, indicating the coalescence of neighboring smaller bubbles to form larger bubbles. This can be confirmed by the significant increase in N_b for bubble size diameter, D_b of 100–160 mm for the original bed ($d_p = 1.0$ mm) and 60 – 120 mm for the SPA bed ($d_{p'} = 3.0$ mm). Despite the ability to accurately simulate most of the bubble sizes of the original bed ($d_p = 1.0$ mm), the N_b of the SPA bed ($d_{p'} = 3.0$ mm) is approximated to be relatively smaller. On the other hand, the magnification in the SPA bed ($d_{p'} = 6.0$ mm) is far too large to yield results similar to those for the original bed ($d_p = 1.0$ mm), i.e., resulting in smaller N_b for bubble

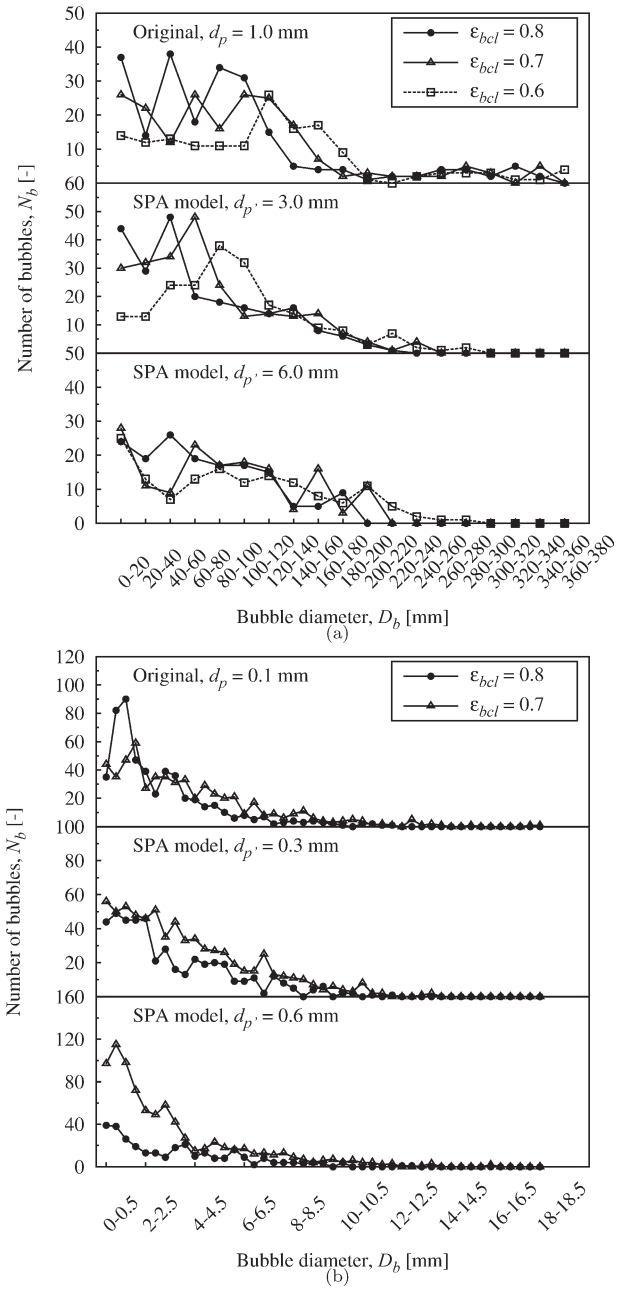

Figure 7. Comparison of bubble size distributions between the original bed and the SPA beds obtained at various bubble voidage constant lines for (a) Geldart's Group D particles and (b) Geldart's Group A particles.

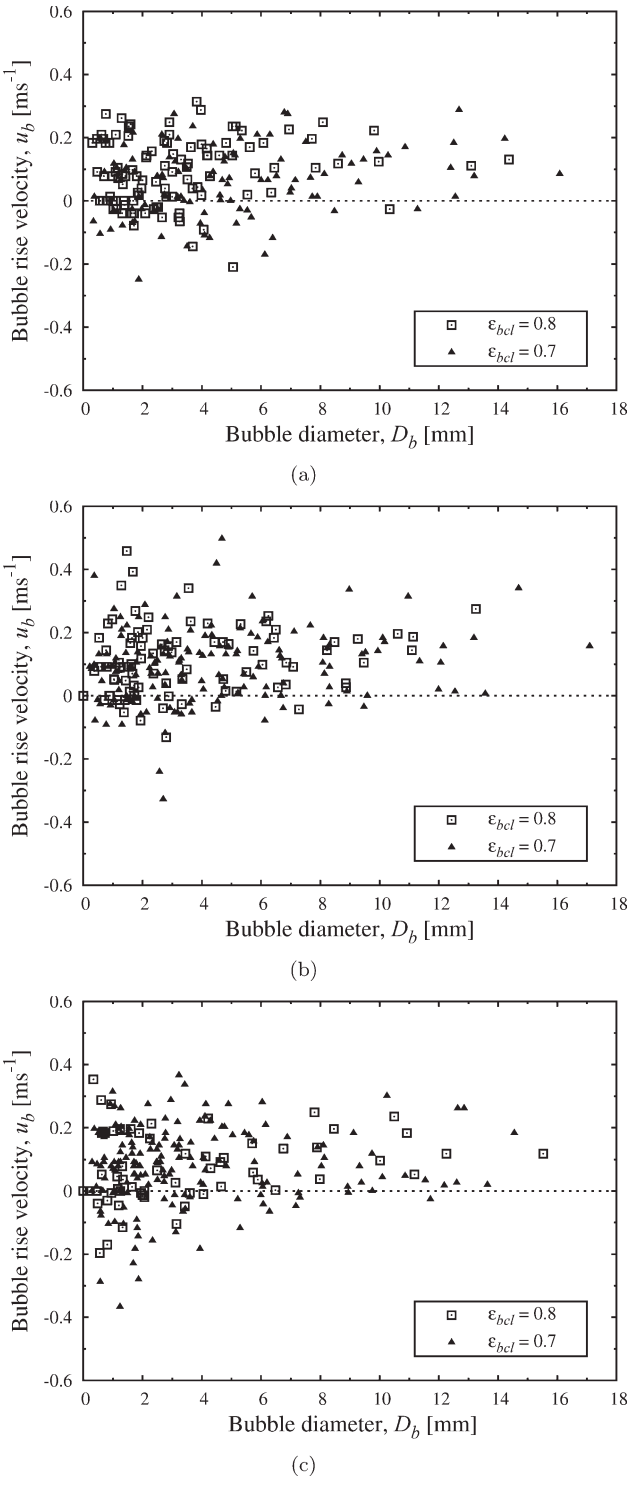

Figure 8. Comparison of bubble rise velocity between (a) the original bed (d_p = 0.1 mm), (b) the SPA model ($d_{p'}$ = 0.3 mm), and (c) the SPA model ($d_{p'}$ = 0.6 mm) during bubbling fluidization (u_0 = 0.03 m/s) of Geldart's Group A particles.

sizes of range 0–120 mm. N_b also becomes less affected by ε_{bcl} variances. Figure 7b shows the bubble analysis performed for Geldart's Group A particles. This type of particle usually has a small bubble diameter-to-bed width ratio. Here, the SPA beds ($d_{p'}$ = 0.3, 0.6 mm) exhibit identical bubble sizes to the original bed, but with a relatively smaller number of bubbles. The original bed (d_p = 0.1 mm) exhibits a rather steady gradient distribution, which is closely approximated by the SPA bed ($d_{p'}$ = 0.3 mm). In addition, the narrow fluctuation amplitude of N_b observed in the SPA beds ($d_{p'}$ = 0.3, 0.6 mm) indicates that the bubbles are nearly uniform in size, which is similar to the results for the original bed (d_p = 0.1 mm). In addition, when the representative particle diameter becomes too large in the SPA model, it exceeds ε_{bcl}, which causes the empty spaces formed between particles to be recognized as bubbles. For example, in the SPA bed ($d_{p'}$ = 0.6 mm), when ε_{bcl} = 0.7, the maximum value of N_b becomes nearly twice as large as the value for other models for D_b below 4.0 mm. As mentioned in "Influence of Voidage variations on the bubble size distribution" section, for Group A particles, bubbles can be very difficult to recognize when ε_{bcl} is below 0.7. Thus, the results for ε_{bcl} = 0.6 are not presented herein.

Figure 8 shows the relationship between the bubble diameter D_b and the bubble rise velocity u_b for both the original bed and the SPA beds, analyzed for Geldart's Group A only, because a relatively large number of bubbles is present. The results are plotted with respect to two values of ε_{bcl}. In the original bed (d_p = 0.1 mm), the distribution of small bubbles at low bubble rise velocities is extremely dense. This is expected because small bubbles rise more slowly through the bed than large bubbles. The negative value of u_b indicates that some of the bubbles move downward as a result of interactions with larger bubbles (or wakes) that rise in a swarm pattern. For the SPA bed with 0.3-mm particles, a similar distribution can be observed, except that, here, the bubbles are predominantly concentrated at positive u_b. Here, the number of bubbles N_b is smaller compared to that of original bed, resulting in a reduced effect of bubble-bubble interactions, i.e., the bubbles can rise upward more easily, some with a slightly higher velocity u_b. The overestimated N_b when ε_{bcl} = 0.7 in the SPA bed ($d_{p'}$ = 0.6 mm), as described earlier, resembles the result for the original bed, where some of the bubbles shift to negative u_b. In addition, the variations in ε_{bcl} has less of an effect on D_b and N_b, and thus only small increases in u_b are observed in the original bed (d_p = 0.1 mm) and the SPA beds ($d_{p'}$ = 0.3, 0.6 mm).

Cohesive particles fluidization

In the fluidization of cohesive (wet) particles, the cohesive force equation was used in the force balance equation for the particle phase to model the liquid bridge forces $\boldsymbol{F}_{coh}$ between particles of Geldart's Group D. During fluidization, the gas velocity u_0 increased linearly to 1.2 m/s until t = 0.26 s, remained constant at 1.2 m/s until t = 3.23 s, and then decreased linearly to 0 m/s at t = 5.23 s to measure the minimum fluidizing velocity u_{mf}. Figure 9 shows snapshots of the wet-particle fluidization of the original bed (d_p = 1.0 mm) and the SPA beds (d_p = 3.0, 6.0 mm). In Figure 9a, identical plug flow structures are observed at t = 0.79 s for the original bed and the SPA beds. Here, pillar-shaped particle plugs can be observed in all beds. However, the top plugs of the SPA beds ($d_{p'}$ = 3.0, 6.0 mm) in the snapshots between t = 0.79 – 1.31 s break earlier than in the original

bed (d_p = 1.0 mm) at t = 1.31 s, as shown in Figure 9b. This earlier breakage is caused by the increase in the weight of particles as the magnification becomes larger in the SPA model. In all of the beds, just before plug breakage, agglomerates can be observed below the top plugs. The agglomerate size in the SPA beds ($d_{p'}$ = 3.0, 6.0 mm) is slightly larger than in the original bed (d_p = 1.0 mm). However, the diffusion behavior of particles and the bubble size of the SPA beds are relatively similar. Figure 10 shows the mixing behavior based on the average height of lower-half set particles during wet fluidization. While the SPA bed ($d_{p'}$ = 3.0 mm) agreed well with the original bed (d_p = 1.0 mm), the agreement between the original bed and the SPA bed ($d_{p'}$ = 6.0 mm) from t = 1.50 was poor. However, the original bed and the SPA bed ($d_{p'}$ = 6.0 mm) gradually become comparable starting from t = 3.50 s. To the best knowledge of the authors, this would be the first successful numerical simulation of the fluidization of cohesive particles using a model to reduce the number of particles.

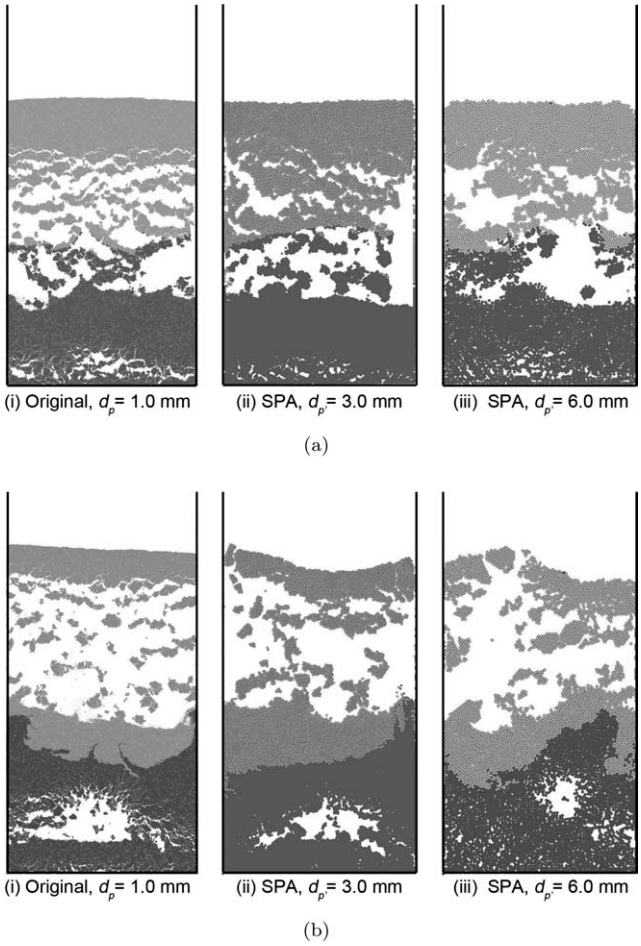

Figure 9. Comparison of fluidization behavior for Group D particles during (a) plug formation and (b) plug breakage between the original bed (d_p = 1.0 mm) and the SPA beds, ($d_{p'}$ = 3.0, 6.0 mm).

Cohesive force is modeled by liquid bridge force $\boldsymbol{F}_{coh}$ with dimensionless liquid volume $\hat{V}$= 1.0 × 10^{-2}.

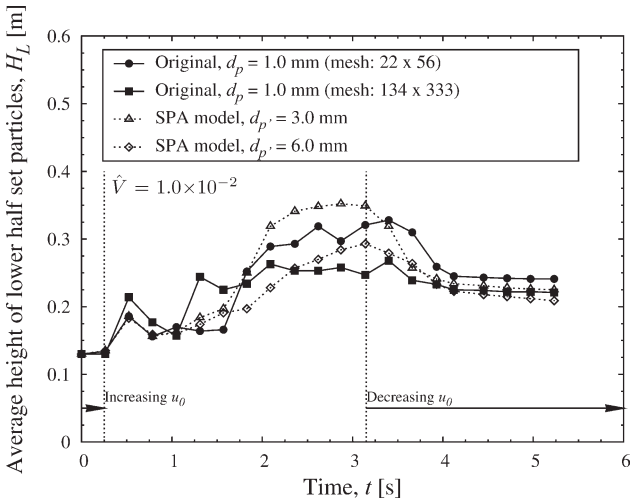

Figure 10. Average height of lower-half set particles during cohesive fluidization of Group D particles.

Conclusion

The SPA model was validated for the large-scale DEM simulation. The DEM incorporated with the SPA model and the normal DEM calculation were compared in terms of macro- and meso-scale fluidization behaviors. Solid particles of Group A and Group D from Geldart's particle classification were chosen and were fluidized under the noncohesive (dry) and cohesive (wet) bed operations. Several important results were obtained:

The fluidization behaviors, such as slug flow, bubbling flow, splashing, and mixing breakthrough, during the fluidization simulated by the SPA model for the case of Geldart's Group D (d_p = 1.0 mm) particles were similar, although differences did exist. The formation of solid plugs and the agglomerate size were similar in the fluidization of cohesive particles.

The homogeneous fluidization of Geldart's Group A (d_p = 0.1 mm) particles simulated by the SPA model was similar, although mixing breakthrough occurred slightly later than in the original bed.

The bubble size distribution was approximately the same for the SPA model with three times magnification and the original bed. However, the bubble size distribution was poorly predicted by the SPA model with six times magnification, in which only a small number of bubbles were detected.

Based on these results, the validity and applicability of the SPA model were confirmed. However, the limit of magnification in the SPA model should be set to approximately three to retain a favorable approximation of the fluidization characteristic with the bed simulated with the original particle diameter. In addition, in the SPA model, any model can be used for the particle–particle or fluid-particle interaction forces, if it can be used in the standard DEM simulation.

Acknowledgments

This was supported in part by the Ministry of Education, Cultural, Sports, Science and Technology of Japan through the Financial Assistance Program of the Social Cooperation Study (2006–2010).

Notation

d_p = particle diameter [m]
$\boldsymbol{F}_{fp}$ = fluid-particle interaction (drag) force per unit volume [N/m^3]
$\boldsymbol{F}_{coh}$ = cohesive force [N]
$\boldsymbol{F}_f$ = fluid force [N]
$\boldsymbol{F}_n$ = normal contact force [N]
$\boldsymbol{F}_p$ = particle-particle interaction (contact) force [N]
$\boldsymbol{F}_t$ = tangential contact force [N]
$\boldsymbol{g}$ = gravitational acceleration [m/s^2]
h_c = dimensionless rupture distance between particles
I = moment of inertia of the particle [kgm^2]
k_n = normal stiffness [N/m]
k_t = tangential stiffness [N/m]
m = integer magnification factor
N_p = particle number
ΔP = bed pressure drop [Pa]
r_p = particle radius [m]
$\boldsymbol{v}_i$ = i-th particle velocity [m/s]
$\boldsymbol{x}_n$, $\boldsymbol{x}_t$ = overlap distance between the interacting particles [m]

Greek letters

γ_c = surface tension [N/m]
η = viscous damping coefficient [N s/m]
ε = fluid phase (gas) voidage
ε_{bcl} = voidage at the bubble boundary line
μ = friction coefficient
μ_f = fluid viscosity [Pa s]
ρ_f = fluid density [kg/m^3]
ρ_p = particle density [kg/m^3]
ω = angular velocity [rad/s]

Subscripts

i,j = particle indices/identifiers in Euclidean space
n = normal direction
p = particle
t = tangential direction

Superscript

*, $'$ = representative indicators in the m-times larger system

Literature Cited

1. Cundall PA, Strack ODL. Discrete numerical model for granular assemblies. *Geotechnique*. 1979;29–1:47–65.
2. Kuwagi K, Horio M. A numerical study on agglomerate formation in a fluidized bed of fine cohesive particles. *Chem Eng Sci*. 2002; 57:4737–4744.
3. Hoguea MD, Callea CI, Curryb DR, Weitzmanc PS. Discrete element modeling (DEM) of triboelectrically charged particles: revised experiments. *J Electrostat*. 2009;67:691–694.
4. Tsuji Y, Kawaguchi T, Tanaka T. Discrete particle simulation of two-dimensional fluidized bed. *Powder Technol*. 1993;77:79–87.
5. Mikami T, Kamiya H, Horio M. Numerical simulation of cohesive powder behavior in fluidized bed. *Chem Eng Sci*. 1998;53:1927–1940.
6. Kuwagi K, Mikami T, Horio M. Numerical simulation of metallic solid bridging particles in fluidized bed at high temperature. *Powder Technol*. 2000;109:27–40.
7. Kuczynski GC. Diffusion in sintering of metallic particles. *Metals Trans*. 1949;185:169.
8. Rong D, Horio M. DEM simulation of char combustion in a fluidized bed. Presented at the 2nd International Conference on CFD in the Minerals and Process Industries, Melbourne, Australia, 1999;65–70.
9. Iwadate Y, Horio M. Prediction of agglomerate sizes in bubbling fluidized beds of group C powders. *Powder Technol*. 1998;100:223–236.
10. Rong D, Mikami T, Horio M. Particle and bubble movements around tubes immersed in fluidized beds: a numerical study. *Chem Eng Sci*. 1999;54:5737–5754.
11. Kaneko Y, Shiojimaa T, Horio M. DEM simulation of fluidized beds for gas-phase olefin polymerization. *Chem Eng Sci*. 1999;54: 5809–5821.
12. Gordon M. Progress in digital integrated electronics. *IEEE, IEDM Tech Digest*. 1975:11–13.
13. Schaller R. Moore's law: past, present, and future. *IEEE Spectrum*. 1997;34:52–59.
14. Tsuji T, Yabumoto K, Tanaka T. Spontaneous structures in three-dimensional bubbling gas-fluidized bed by parallel DEM-CFD coupling simulation. *Powder Technol*. 2008;184:132–140.
15. Keyes DE, Kaushik DK, Smith BF. Prospects for CFD on petaflops systems. Technical Report TR-97–73, Institute for Computer Applications in Science and Engineering, 1997.
16. Kuipers, JAM, van Duin KJ, van Beckum FPH, van Swaaij WPM. A numerical model of gas-fluidized beds. *Chem Eng Sci*. 1992; 47:1913–1924.
17. Kazari M, Roko K, Kawaguchi T, Tanaka T, Tsuji Y. A Study on conditions for similarity of particle motion in numerical simulation of dense gas-solid two phase flow. In: A. Serizawa, T. Fukano, J. Battaille, editors. Proceedings of The 2nd International Conference on Multiphase Flow, Kyoto, Japan: Elsevier Science Ltd. 1995;(FB2–9)–(FB2–15).
18. Sakano M, Yaso T, Nakanishi H. Numerical simulation of two-dimensional fluidized bed using discrete element method with imaginary sphere model. *Jpn J Multiphase Flow*. 2000;14:66–73.
19. Takeda H, Horio M. The particulate object simulation according to the hybrid model of continuum modeling and DEM. In: Proceedings of the SCEJ Symposium on Fluidization, Japan: Society of Chemical Engineers (SCEJ). 2000;6:162–167.
20. Snider D. M. An incompressible three-dimensional multiphase particle-in-cell model for dense particle flows. *J Com Phys*. 2001;170: 523–549.
21. Benyahia S, Galvin JE. Estimation of numerical errors related to some basic assumptions in discrete particle methods. *Ind Eng Chem Res*. 2010;49:10588–10605.
22. Kuwagi K, Takeda H, Horio M. The similar particle assembly (SPA) model: an approach to large-scale discrete element (DEM) simulation. Presented at the International Conference on Fluidization Engineering XI, Ischia, Naples, 2004:243–250.
23. Sakai M, Koshizuka S. Large-scale discrete element modeling in pneumatic conveying. *Chem Eng Sci*. 2009;64:533–539.
24. Sakai M, Yamada Y, Shigeto Y, Shibata K, Kawasaki VM, Koshizuka S. Large-scale discrete element modeling in a fluidized bed. *Int J Numer Meth Fluids*. 2010;64:1319–1335.
25. Anderson TB, Jackson R. A fluid mechanical description of fluidized beds. *I & EC Fundamentals*. 1967;6:527–539.
26. Mikami T. Agglomerating fluidization of liquid/solid bridging particles and its control. PhD thesis, Tokyo University of Agricultural and Technology, 1998.
27. Fisher RA. On the capillary forces in an ideal soil; correction formulae given by Haines WB. *J Agric Sci*. 1926;16:492.
28. Mason G, Clark WC. Liquid bridge between spheres. *Chem Eng Sci*. 1965;20:859.
29. Ennis BJ, Li J, Tardos GI, Pfeffer R. The influence of viscosity on the strength of an axially strained pendular liquid brigde. *Chem Eng Sci*. 1990;45:3071.
30. Lian G, Thornton C, Adams MJ. A theoretical study of the liquid bridge forces between two rogid spherical bodies. *J Colloid Interface Sci*. 1993;161:138.
31. Kuwagi K, Mokhtar MA, Okada H, Hirano H, Takami T. Numerical experiment of thermoset particles in surface modification system with discrete element method (Quantization of cohesive force between particles by agglomerates analysis). *Numer Heat Transfer, Pt A: Apps*. 2009;56:647–664.
32. Geldart D. Types of gas fluidization. *Pow Tech*. 1973;7:285.
33. Wen CY, Yu YH. Mechanics of fluidization. *Chem Eng Prog Symp*. 1966;62:100–111.
34. Ergun S. Fluid flow through packed columns. *Chem Eng Prog*. 1952;48:89–94.
35. Patankar SV, Spalding DB. A calculation procedure for heat, mass and momentum transfer in three-dimensional parabolic flows. *Int J Heat Mass Trans*. 1972;15:1787–1806.
36. Shapiro LG, Stockman GC. *Computer Vision*. Upper Saddle River, NJ: Prentice Hall, 2001:83–89.
37. Li J, Kuipers JAM. Effect of competition between particle-particle and gas-particle interactions on flow patterns in dense gas-fluidized beds. *Chem Eng Sci*. 2007;62:3429–3442.

38. Girimonte R, Formisaniy B. *Effects of thermally induced interparticle forces on the expansion and bubbling behaviour of a fluidized bed*. In: Franco B, Xiaotao TB, Todd P, Eds. *Proceedings of the 2007 ECI Conference on The 12th International Conference on Fluidization*, 2007;RP4:177–184.
39. Rietema K. *The Dynamics of Fine Powders*. Amsterdam: Elsevier, 1991.
40. Foscolo PU, Gibilaro LG. A fully predictive criterion for the transition between particulate and aggregate. *Chem Eng Sci*. 1984;39:1667–1675.
41. Valverde, JM, Castellanos A, Quintanilla MAS. Self-diffusion in a gas-fluidized bed of fine powder. *Phys Rev Lett*. 2001;86:3020–3023.
42. Toomey RD, Johnstone HF. Gaseous fluidization of solid particles. *Chem Eng Prog*. 1952;48:220–226.
43. Oka SN, Anthony EJ. *Fluidized Bed Combustion*. New York: Marcel Dekker, 2004.
44. Zhang Y, Jin B, Zhong W. Experimental investigation on mixing and segregation behaviour of biomass particle in fluidized bed. *Chem Eng Proc: Process Intensification*. 2009;48:745–754.
45. Bosma JC, Hoffmann AC. Feasibility study of particle classification in fluidized beds with internal baffles. In: Proceedings WCPT4, the Fourth World Congress on Particle Technology, Sydney, 2002.

Manuscript received Mar. 7, 2010, and revision received Dec. 12, 2010.